Noncontact Power Meter

John S. Donnal, *Member, IEEE*, and Steven B. Leeb, *Fellow, IEEE*

***Abstract*— Energy metering is increasingly important in today's power grid. With real-time power meters, utilities can efficiently incorporate renewables and consumers can tailor their demand accordingly. Several high-profile attempts at delivering realtime energy analytics to users, including Google Power Meter and Microsoft Hohm, have essentially failed because of a lack of sufficient richness and access to data at adequate bandwidth for reasonable cost. High performance meters can provide adequate data, but require custom installation at prohibitive expense, e.g., requiring an electrician for installation. This paper presents hardware and signal processing algorithms that enable high bandwidth measurements of voltage, current, harmonics, and power on an aggregate electrical service (such as a residential powerline) for nonintrusive analysis with hardware that requires no special skill or safety considerations for installation.**

***Index Terms*— Smart meter, load monitoring, hall effect, tunneling magnetoresistance.**

I. INTRODUCTION

MONTHLY power bills do not communicate the time varying cost of electric power generation and do not provide a breakdown of consumption per appliance. Providing this type of feedback generally involves the installation of intrusive current or voltage sensors or access to diagnostics "designed in" during construction of a drive or similar load.

Recent studies have shown that households with real time energy meters consume an average of 3.8% less power than those with standard meters [1]. A "smart meter" that communicates with the utility enables even more effective cost savings because the utility can dynamically price consumption at the marginal cost of production, encouraging consumers to reduce demand during peak load times [2]. For these reasons, the GO 15, an international organization of the world's largest Power Grid Operators, has prioritized investment in improved power monitoring technology [3]. Unfortunately the financial and logistical difficulties of installing such power meters has limited their adoption by utilities and their customers [2].

Unlike traditional power meters that require an electrician to install, or must be built in to a product, non-contact sensors can be easily installed by the end user with no service interruption. This enables easier access to electrical consumption information for energy score keeping, diagnostics, and control. Sensors can be placed on the outside of a circuit breaker box, around the service entry cable, or on any electric cord. Conductors do not have to be separated, voltage and current can be measured simultaneously, and it is not necessary to geometrically surround conductors with any material. This ease of installation enables exciting possibilities for agile power monitoring.

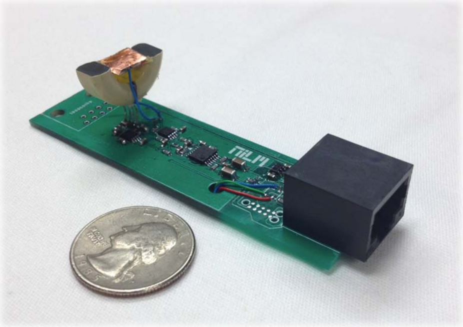

Fig. 1. A non-contact sensor that can measure electric power consumption with no ohmic contact or access to isolated conductors.

This paper presents three key elements of a system for non-contact power metering. These elements include (a) circuit designs for voltage and current sensors with the required sensitivity, (b) a method to disaggregate the currents from multiple conductors that are in close proximity, and (c) a sensor calibration procedure which allows users to arbitrarily place non-contact sensors and retrieve accurate power measurements, all without any service interruption.

II. THE NEED FOR NON-CONTACT MONITORING

Measuring electric power consumption requires current and voltage sensing. There are many current and voltage sensors available but they generally require significant installation effort. Voltage sensors may involve an ohmic contact. Current sensors often require separated access to each conductor, and may require the conductor of interest to be completely surrounded by a magnetic material. In many environments installing such sensors requires a service interruption and potential exposure to high voltage conductors.

In environments with high "up time" requirements and mission critical equipment, retrofitting power monitors is especially challenging. On military forward operating bases (FOB's) electrical requirements change quickly as tenant units add and remove equipment depending on their particular mission. Requiring an electrician to disconnect all power and install sensors each time new equipment is added or removed from the FOB is not a feasible solution. With non-contact sensors (see Figure 1) , any power cable or breaker panel can become a power monitoring node and when a cable or panel is

---

Manuscript received August 20, 2014; revised September 1, 2014; accepted September 1, 2014. Date of publication September 19, 2014; date of current version December 3, 2014. This work was supported in part by the Grainger Foundation, in part by the Martin Foundation, and in part by the a grant from the Massachusetts Institute of Technology Energy. The associate editor coordinating the review of this paper and approving it for publication was Dr. E. H. Yang.

The authors are with the Massachusetts Institute of Technology, Cambridge, MA 02139 USA (e-mail: jdonnal@mit.edu; sbleeb@mit.edu).

Color versions of one or more of the figures in this paper are available online at http://ieeexplore.ieee.org.

Digital Object Identifier 10.1109/JSEN.2014.2359619

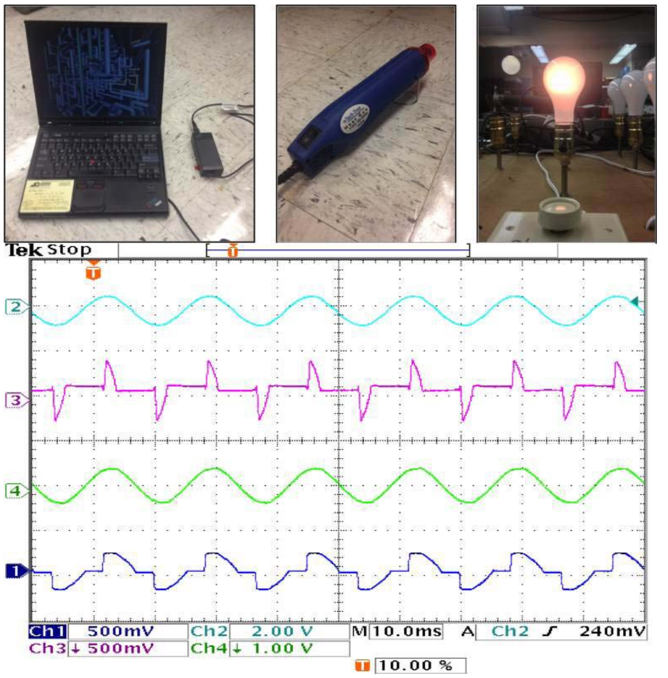

Fig. 2. Measuring common electric loads with non-contact sensors. The top trace is the voltage common to all loads. The second, third and fourth traces are the current waveforms drawn by the appliances pictured (in order from left to right).

no longer a target of interest, the sensors can be easily moved to a new location.

In addition to being able to measure aggregate consumption, these non-contact sensors have sufficient bandwidth to resolve the high order harmonics that characterize many power electronic devices and motors. This high resolution coupled with the low cost of installation makes these sensors ideal for non-intrusive load monitoring (NILM). NILM uses characteristic transients in current to determine which kinds of appliances or other loads are using power at a given time. To date research in NILM techniques has focused mainly on the non-intrusiveness of algorithms rather than the sensor hardware itself [4]–[6]. Figure 2 shows non-contact sensor measurements for three different loads. The top trace is line voltage which is common to all the loads. The second trace is current from a personal laptop which, like many consumer-grade digital electronics, draws current pulses. The third trace is the current from a heat gun which, as a purely resistive load, is a relatively sinusoidal waveform. The final trace is the current from a light bulb on a phase controlled dimmer. These three exemplars illustrate the variety of current draw in common electric loads and suggest exciting identification and diagnostic applications for non-contact sensor platforms.

III. NON-CONTACT CURRENT SENSING

One of the primary difficulties in non-contact power monitoring is designing a sensor capable of measuring current flow at a distance. Ampere's Law establishes the linear relationship between magnetic fields and current, but without a closed path around the conductor, accurately measuring this magnetic field is a challenging task. On the surface of a circuit breaker and the exterior of a power cable, the magnetic fields are not uniform or symmetric, and depending on the particular geometry, can be very small-less than 1 Gauss for bench top load currents in typical wires. Subsections A and B below introduce two circuit topologies that can accurately sense these small fields and can do so even in the presence of DC offsets introduced by nearby magnetic elements such as steel breaker panels, and the Earth itself. Section V will present a method for reconstructing currents from these field measurements.

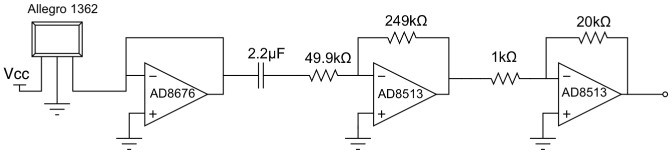

Fig. 3. Schematic of Hall Effect-based current sensor.

The first circuit, based off a Hall Effect sensor is a cost effective solution suitable for measuring larger loads or in situations where the wire topology exposes a relatively strong magnetic field. The second non-contact circuit uses a Tunneling Magnetoresistive (TMR) element (a recently introduced sensor technology [7]) with an inductive feedback technique to accurately measure extremely small fields.

A. Hall Effect Sensor

The schematic for this circuit is shown in Figure 3. The Hall Effect is widely known and used in many current sensor designs. One of the most sensitive devices available in quantity is Allegro MicroSystem's A1362 Hall Effect sensor [8]. The A1362 has a programmable gain which can be set up to 16 mV/G, sufficient to resolve the magnetic fields around a standard power line. The quiescent output level is also programmable but not tightly controlled. Therefore, in order to measure small fields without saturating the output, we add a high pass filter with a cutoff at 1.5 Hz to AC-couple the sensor to the inverting amplifier gain stage. The large capacitive input of the filter stage requires a follower to buffer the sensor output. Overall gain can be adjusted by tuning the feedback leg of the gain stage.

The circuit is evaluated in the experimental setup shown in Figure 4a. A signal generator coupled with a power amplifier drives a solenoid at 200Hz to generate a magnetic field around the sensor. The circuit's output is compared to the field strength as measured with a fluxgate-magnetometer (an Aim Instrument I-prober 520). Results are shown in Figure 5. Two levels of field strength illustrate the degree of hysteresis in the sensor response. Steeper slope reflects higher sensitivity.

In situations where the geometry of the fields is approximately known, the response of the Hall Effect circuit can be improved by attaching magnetic material parallel to the field lines around the A1362 chip. The prototype in Figure 1 uses two ferrite segments to form a partial torus around the sensor package. This geometry captures radial fields near the surface of a multiconductor cable such as the three phase power line in Figure 16.

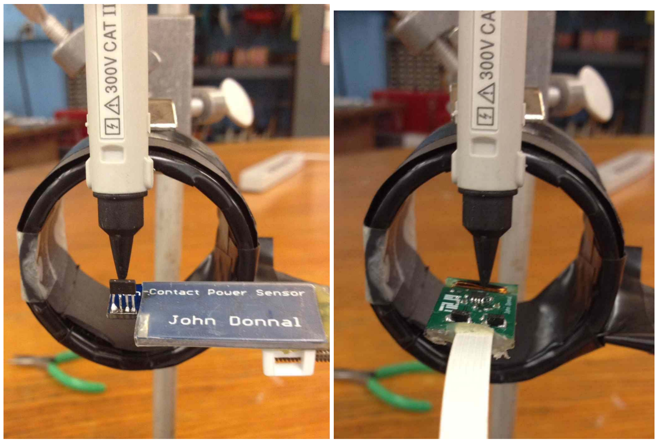

(a) (b)

Fig. 4. Non-contact current sensors are placed in an air core solenoid to evaluate their sensitivity and linearity to applied magnetic fields. (a) Hall Effect Sensor. (b) Compensated TMR Sensor.

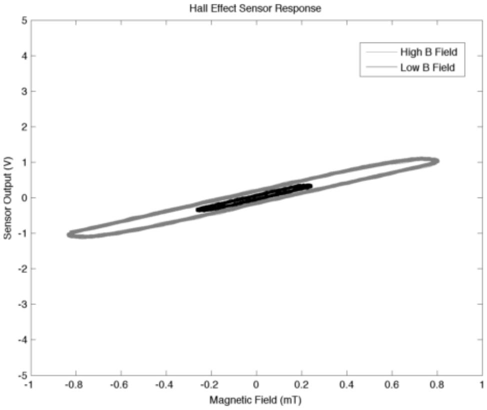

Fig. 5. Response of Hall Effect-based sensor to applied fields.

B. Tunneling Magnetoresistive Sensor

The TMR effect describes the change in resistance of a particular material due to applied magnetic fields. An explanation of the effect was first published in the 1970's but garnered little interest because practical implementations generated relatively small changes in material resistance [9]. Recent advancements using new materials and advanced fabrication techniques have improved the sensitivity of TMR devices. Modern state of the art sensors have a tunnel magnetoresistance of over 600% at room temperature [10], [11]. Interest in these devices has increased as they have become integrated into high density magnetic disk drives and MRAM [12].

The STJ-340 is a TMR Wheatstone bridge sensor produced by MicroMagnetics. The sensor has four active TMR elements, arranged in a Wheatsone bridge architecture. Changes in the field induce an imbalance in the bridge which can be measured by a differential amplifier [7]. While the STJ-340 can detect very small fields (25mV/G as constructed), there are two significant challenges in using it as a current sensor. First, as with the Hall Effect-based sensor, DC offset errors quickly saturate the sensor output. The offset errors from the environment and from imbalance in the bridge itself (which can be up to 10%) must be removed before applying any significant gain to the output. More troubling is that the TMR sensor's response to large changes in magnetic field is inconsistent and non-proportional; that is, there is no constant ratio between the change in the magnetic field and the resulting change in the sensor output. the sensor's nonlinear response to large changes in the applied field. Figure 6 compares the true current as measured by a commercial current sensor (an LEM LA-55-P) to the output of an uncompensated TMR-based sensor. Even with proper amplification and DC offset removal, step changes in the load current produce non-linear responses in the sensor output.

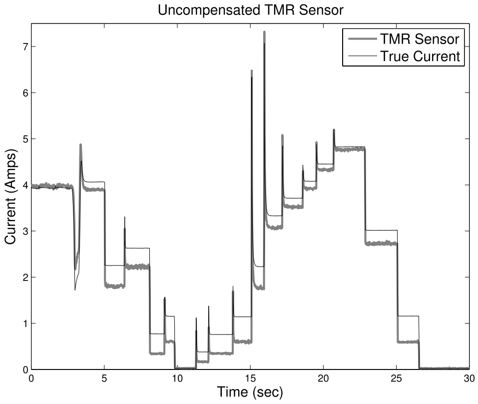

Fig. 6. Non-linear response of an uncompensated TMR-based sensor. The sensor does not have a consistent response to a given change in current.

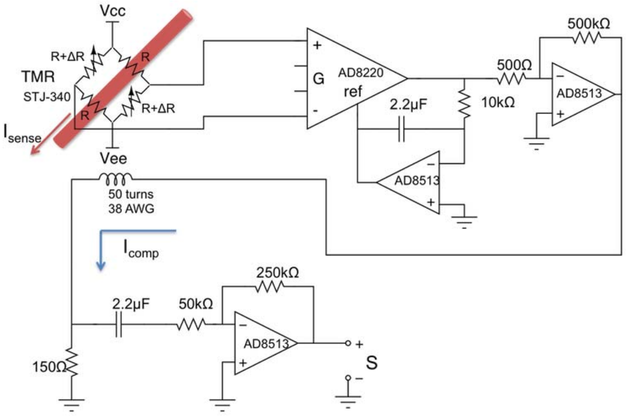

Fig. 7. Schematic of the compensated TMR-based current sensor.

The circuit shown in Figure 7 addresses both the DC offset and the non-linearity problems of the TMR sensor. The DC offset error is corrected by an integrator connected to the REF pin of the instrumentation amplifier. Any DC component is subtracted off the amplifier output resulting in a purely AC signal. This output is then fed through a high gain stage which drives an air core solenoid wrapped around the STJ-340. The current through this solenoid builds a magnetic field that opposes the applied field, creating a feedback loop that zeros the operating point of the STJ-340. Keeping the sensor element exposed to very small fields improves the sensor linearity and increases its range of operation. The current driven in the

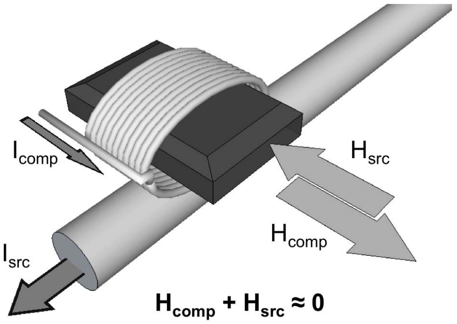

Fig. 8. Illustration of TMR feedback technique.

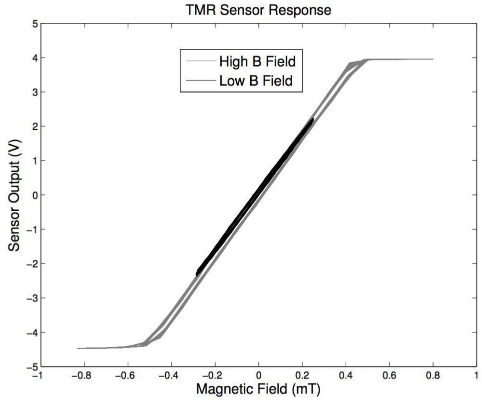

Fig. 9. Response of compensated TMR-based sensor to applied fields.

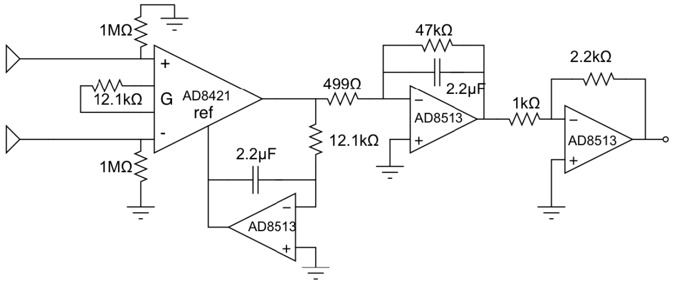

Fig. 10. Non-contact voltage sensor schematic.

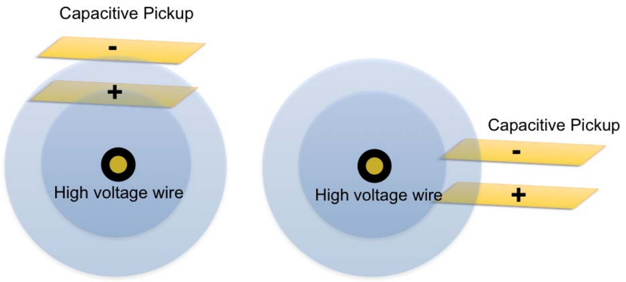

(a) (b)

Fig. 11. Differential design concentrates the gain below the sensor. (a) Differential mode. (b) Common mode.

compensation solenoid is sensed as a voltage across a 150Ω resistor. The final stage is a high pass filter and gain stage that removes any offset not compensated for in the integrator.

The conceptual operation of the feedback topology is shown in Figure 8. In steady state operation the sensed H_{src} and driven H_{comp} fields are approximately equal and the TMR element is exposed to only a very small residual field. The air core solenoid has proven remarkably effective because closed-loop feedback is used to control the compensation coil.

The circuit is evaluated using the same procedure as the Hall Effect circuit. The experimental setup is presented in Figure 4b. The results in Figure 9 show the high sensitivity (relative to the Hall Effect sensor in Figure 5) and linear response of the compensated TMR-based sensor. The saturation effects are due to the power rails and not the operation of the circuit itself. The hysteresis in the high field data series is also a result of the power rail limits. The feedback loop cannot drive sufficient current to eliminate the magnetic field at the sensor surface thus exposing the TMR's inherent non-linearities.

IV. NON-CONTACT VOLTAGE SENSING

While the amplitude of the voltage is usually known in a standard power grid (eg 120V), the phase must be measured in order to calculate real and reactive power. In order to measure the voltage without making ohmic contact, a capacitive pickup can be used to sense the electric field. By measuring the voltage this field induces on the pickup, it is possible to calculate the voltage of the conductor itself. The full non-contact voltage sensor schematic is shown in Figure 10. The differential inputs to the instrumentation amplifier are connected to two copper foil plates which serve as capacitive pickups. The 1MΩ resistor provides input bias current to the amplifier while maintaining the high impedance required to build up voltage on the pickup due to the surrounding field. This input stage forms an RC divider with a transfer function of

$$H(s) = \frac{sRC}{1 + sRC} \tag{1}$$

While the resistance is high, on the order of the bias resistor, the capacitance is very small, estimated to be on the order of a few picofarads, so the quantity $sRC \ll 1$, and the transfer function reduces to sRC. In order to compensate this undesired frequency response, the instrumentation amplifier is followed by an integrator. As with the non-contact current sensor, any DC offset leads to saturation at the gain stage so the same feedback technique is used to remove any differential mode DC offset between the pickups. The final stage is a standard inverting amplifier.

The electric field can be measured using a single ended topology but a differential design increases the performance with minimal increase in complexity. In an environment with many different high voltage conductors, a single foil pickup acts as an omnidirectional sensor. By using a differential setup the sensor can be directionally targeted to the region of interest. Figure 11 illustrates the differential sensor operation. Conductors directly below the sensor generate higher magnitude fields on the bottom plate than on the top plate while conductors to the sides of the sensor generate equal magnitude fields on both plates. The differential amplifier rejects the common mode signals providing selectively higher

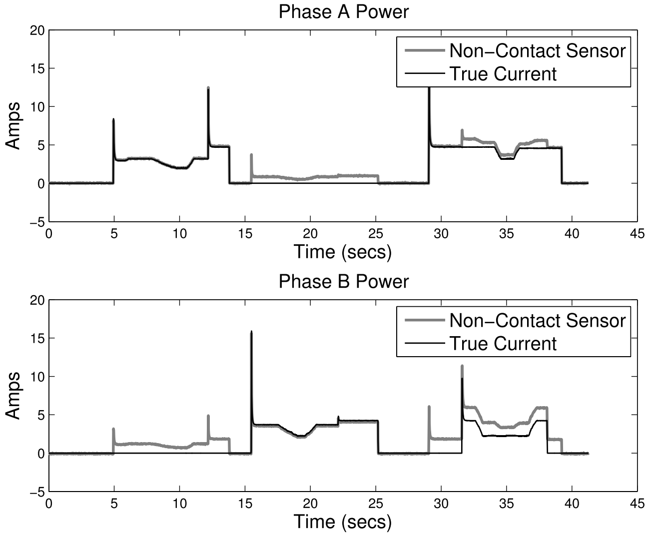

Fig. 12. Comparing actual current to Hall Effect non-contact sensors on a multiconductor cable. Interfering magnetic fields the corrupt non-contact sensor measurements.

gain to conductors located below the sensor surface. See [13] for additional analysis of the sensor operation.

V. Monitoring Multiple Conductors

In many systems of interest there are multiple current-carrying conductors. If the magnetic fields of the conductors overlap, the output of any single non-contact sensor will be a combination of these fields, misrepresenting the current flowing in the nominal conductor of interest. Figure 12 compares the output of Hall Effect non-contact sensors to traditional LEM current sensors on two conductors in close proximity. Each non-contact sensor picks up significant interference from current in the neighboring conductor. This section introduces techniques to accurately measure individual currents with non-contact sensors in environments with complex, superposed magnetic fields.

A. Monitoring a Circuit Breaker Panel

Due to the close proximity of circuits on a breaker panel and the steel construction of the panel itself, the magnetic fields are often fully mixed so that any single sensor detects some portion of every current flowing through the panel or cable. Even if a precise location for minimal interference could be determined, the narrow dimensions of many breaker panels limit placement options as seen in Figure 13. Assuming the breaker currents are linearly independent, the number of sensors (X) must be equal to the number of breakers (Y) in order to calculate the currents in the panel. The x^{th} sensor output for such a system can be expressed as:

$$S_x = M_{x1}I_1 + M_{x2}I_2 + \cdots + M_{xY}I_Y \tag{2}$$

Or, equivalently using the inverse relationship, the y^{th} breaker current can be expressed as:

$$I_y = K_{1y}S_1 + K_{2y}S_2 + \cdots + K_{Xy}S_X \tag{3}$$

The full system can be expressed in matrix form where the current flowing in the breaker directly under each sensor is represented by the diagonal K values and the interference terms are the off-diagonal K's.

Fig. 13. Monitoring a circuit breaker panel with TMR sensors.

$$\begin{bmatrix} I_1 \\ I_2 \\ I_3 \\ \vdots \end{bmatrix} = \begin{bmatrix} K_{11} & K_{12} & K_{13} & \\ K_{21} & K_{22} & K_{23} & \\ K_{31} & K_{32} & K_{33} & \ldots \\ & \vdots & & \end{bmatrix} \times \begin{bmatrix} S_1 \\ S_2 \\ S_3 \\ \vdots \end{bmatrix} \tag{4}$$

B. Monitoring Cables with Neutral Return Path

The equations are slightly different for a multiple conductor power cables. These systems do not have fully independent conductors and are subject to the additional constraint of Kirchoff's Current Law (KCL):

$$I_1 + I_2 + I_3 + \cdots + I_{neutral} = 0 \tag{5}$$

This equation reduces the dimension of the solution space. Standard power cables have only two current-carrying wires-hot and neutral. In this simple case only a single sensor is needed. The equations to find current are:

$$\begin{aligned} I_{hot} &= KS \\ I_{neutral} &= -I_{hot} \end{aligned} \tag{6}$$

The same technique can be extended for multiple phases and a common neutral. For a three phase power cable, such as the one shown in Figure 16, there are four current carrying wires so the full matrix has 16 elements but KCL reduces the number of unknown currents by one. A nine element matrix using only three sensors is enough to determine all the currents. The equations for a three phase power cable are:

$$\begin{aligned} \begin{bmatrix} I_1 \\ I_2 \\ I_3 \end{bmatrix} &= \begin{bmatrix} K_{11} & K_{12} & K_{13} \\ K_{21} & K_{22} & K_{23} \\ K_{31} & K_{32} & K_{33} \end{bmatrix} \times \begin{bmatrix} S_1 \\ S_2 \\ S_3 \end{bmatrix} \\ I_{neutral} &= -(I_1 + I_2 + I_3) \end{aligned} \tag{7}$$

C. Example Reconstruction

By applying the fit matrix $[K]$ for the waveforms in Figure 14 the non-contact sensors accurately measure the true current waveforms in each line.

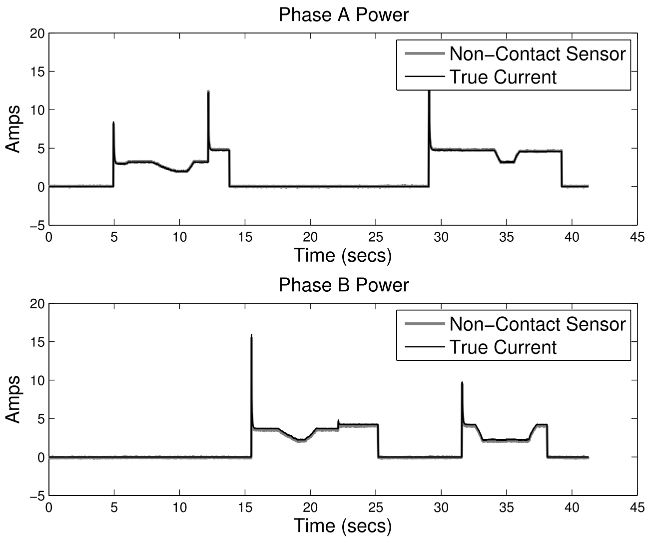

Fig. 14. By applying the appropriate fit matrix interfering magnetic fields can be corrected to correctly measure line currents.

VI. SYSTEM CALIBRATION

Equations (4,6,7) can calculate all currents of interest in complex systems, but they cannot be used until the K_{xy} terms in the fit matrix are determined. If only one current is present, the calibration matrix $[M]$ reduces to a set of equations relating the current to the output of a specific sensor (S_x):

$$\begin{bmatrix} S_1 \\ S_2 \\ S_3 \\ \vdots \end{bmatrix} = \begin{bmatrix} M_{11} & M_{12} & M_{13} & \\ M_{21} & M_{22} & M_{23} & \\ M_{31} & M_{32} & M_{33} & \dots \\ & \vdots & & \end{bmatrix} \times \begin{bmatrix} I_1 \\ 0 \\ 0 \\ \vdots \end{bmatrix}$$
$$\Downarrow \tag{8}$$
$$\begin{aligned} S_1 &= M_{11} I_1 \\ S_2 &= M_{21} I_1 \\ S_3 &= M_{31} I_1 \\ \vdots & \quad\ \vdots \end{aligned}$$

Iterating with a known current on each conductor produces the full matrix $[M]$. The fit matrix can be found as

$$[K] = [M]^{-1} \tag{9}$$

While technically correct, this method places an undue burden on the user to first shut down all connected loads and then connect a single known load to each conductor in sequence. If the system of interest is a circuit breaker panel this type of calibration is unrealistic – a homeowner or facilities manager is unlikely to shut off the power and walk around in the dark connecting test loads. In environments with mission critical equipment, such as a microgrid on an Army FOB, this type of calibration is impossible.

In order to calculate the elements of the $[M]$ matrix without interrupting service, a known current must be separated from the background environment. This can be done by applying pulse width modulation (PWM) to a calibration load to create an identifiable pattern in the current waveform. There are a variety of methods to design a PWM load. Our calibration load tracks the input voltage and draws power for 15 out of every 20 line cycles generating a 75% duty cycle. The full design of the calibration load is presented in [13]. On a 60 Hz service this corresponds to a PWM frequency of 3Hz as shown in Figure 15. Assuming there are no other significant loads cycling at 3Hz, the calibration load can be differentiated from the background environment using spectral analysis. A complete calibration procedure using this PWM load is developed first for a single phase system and then extended for multiphase systems.

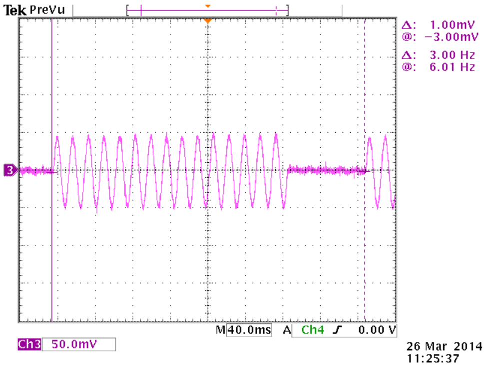

Fig. 15. PWM calibration load as detected by a non-contact sensor.

A. Single Phase Systems

To determine the coefficients of matrix $[M]$ for a given system of conductors, the calibration load is introduced in turn to each of the conductors. In each case, the outputs of the non-contact voltage and currents sensors are fed to a preprocessing algorithm which calculates real and reactive current flow. The preprocessor, fully described in [14] and [15] uses the positive zero crossings of the voltage waveform to compute estimates of real (P) and reactive (Q) current each for line cycle. If all conductors are on the same phase (as in the case of a single phase breaker panel), then the zero crossings of the line voltage correspond exactly to the zero crossings of the non-contact voltage sensors. The calibration load is resistive, drawing purely real power, so only the P output of the preprocessor is used for the calibration procedure.

The preprocessor computes P and Q each line cycle and the calibrator PWM waveform is also defined by line cycles (rather than absolute frequency) which allows the same calibration procedure to be performed on both 50 and 60Hz services and is also robust against line frequency variation during calibration.

If the calibration load is operated in isolation, the real component of the preprocessor output is a line cycle time series that can be defined as follows:

$$P_{cal}[n] = \begin{cases} I_{cal}, & |n| \leq |7| \\ 0, & 7 < |n| \leq 10 \end{cases} \tag{10}$$

and

$$P_{cal}[n+20] = P_{cal}[n]$$

where I_{cal} is the known current draw of the calibration load and n is the line cycle. There is a subtle caveat in the case where the non-contact sensor is 180 degress out of phase with the true current. Since the preprocessor computes P and Q on positive zero crossings the edges of the P_{cal} pulse will

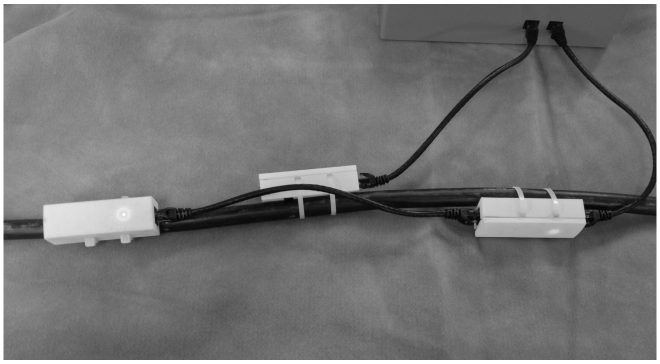

Fig. 16. Monitoring a three phase power line with non-contact sensors.

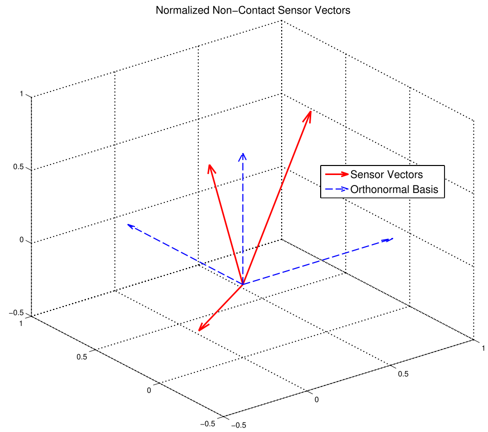

Fig. 17. Visualization on non-contact sensor vectors.

be $0.5I_{cal}$ instead of I_{cal}. In practice this distorition contributes negligible error to the calibration process and can safely be ignored (see Figures 14 and 18).

In a live environment other loads draw arbitrary power throughout the calibration process. Therefore the real component of the preprocessor output for a sensor x is the combination of the calibration load on a conductor y plus an unknown amount of background load:

$$P_x[n] = M_{xy}(P_{cal_y}[n] + P_{bkgd}[n]) \tag{11}$$

where M_{xy} is the unknown scale factor representing non-contact sensor x's response to the calibration load on conductor y and P_{bkgd} is the current drawn by other loads in the system. The goal of this analysis is to find the value of M_{xy}. These coefficients are used to form the matrix $[M]$.

First P_{bkgd} must be removed from the signal. At the harmonics of the calibration waveform, P_{bkgd} is 0 based on the assumption that the calibrator is the dominant load at its PWM frequency. Using the Discrete Fourier Transform (DFT) defined as:

$$\hat{x}[k] = \frac{1}{N}\sum_{n=0}^{N-1} x[n]e^{-2\pi j\frac{kn}{N}} \tag{12}$$

and only considering k's corresponding to harmonics of P_{cal}, the signal measured by the non-contact sensor can be represented in the frequency domain as:

$$\hat{P}_x[k] = M_{xy}\mathcal{F}\{P_{cal_y}[n]\} \tag{13}$$

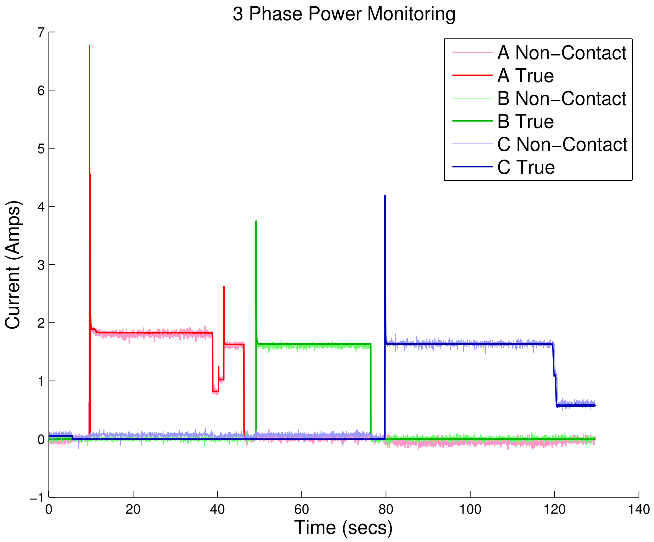

Fig. 18. Hall Effect non-contact sensors and traditional current sensors on a 3 phase system.

Using a 200 point DFT and considering only the fundamental of the calibration waveform, Eq 13 becomes:

$$\hat{P}_x[10] = M_{xy} \times \hat{P}_{cal_y}[10] \tag{14}$$

$\hat{P}_{cal_y}[10]$ is a constant defined by the structure of the calibration waveform. The Fourier Series coefficients of a unit amplitude rectangular pulse with period T and width T_1 are [16]:

$$\begin{aligned} a_k &= \frac{\sin[(2\pi k/T)(T_1+\frac{1}{2})]}{T\sin[2\pi k/2T]}, \quad k \neq 0, \pm T, \pm 2T, \ldots \\ a_k &= \frac{2T_1+1}{T}, \quad k = 0,\ \pm T,\ \pm 2T, \ldots \end{aligned} \tag{15}$$

$P_{cal_y}[10]$ corresponds to term a_1. With the parameters of the load defined in Eq 10:

$$P_{cal_y}[10] = I_{cal}\frac{\sin[3\pi/4]}{20\sin[\pi/20]} \equiv C_1 \tag{16}$$

where C_1 is introduced for notational convenience. Substituting Eq 16 into Eq 14 yields an equation for M_{xy}:

$$M_{xy} = \frac{|\hat{P}_x[10]|}{C_1} \tag{17}$$

The magnitude of $\hat{P}_x[10]$ is required in Eq 14 because the calibration waveform detected by the pickup is actually $P_{cal_y}[n+n_0]$ where n_0 is an uncontrolled time shift due to the fact that the calibration load is not time aligned with the sampling interval. This time shift becomes a phase shift in the frequency domain [17] making $\hat{P}_x[10]$ complex:

$$\hat{P}_x[10] = M_{xy}C_1e^{-jk(2\pi/20)n_0} \tag{18}$$

$$= M_{xy}C_1e^{-j\Phi} \tag{19}$$

where $k = 1$ and Φ is an unknown phase shift. By using only the magnitude in Eq 17 this phase term is eliminated, but the sign of $\hat{P}_x[10]$ is eliminated as well.

Fortunately, the sign can be recovered by using higher harmonics of the calibration waveform. In a 200 point

DFT the second calibration harmonic is present at $\hat{P}_x[20]$. Expressing the second harmonic in the same form as Eq 19 yields:

$$\hat{P}_x[20] = M_{xy} C_2 e^{-j2\Phi} \tag{20}$$

where C_2 corresponds to $\hat{P}_{cal_y}[20]$ which, like C_1, is a constant that can be determined using Eq 10 and Eq 15.

The compensated phase difference between $\hat{P}_x[10]$ and $\hat{P}_x[20]$ can be used to recover the sign of M_{xy}. We define the compensated phase difference between the fundamental and the k^{th} harmonic in a Fourier Series as:

$$\Delta_{ph}(k) \equiv k\angle a_1 - \angle a_k \tag{21}$$

In the case where M_{xy} is positive, the phases of these two terms are:

$$\angle \hat{P}_x[10] = -\Phi \tag{22}$$

$$\angle \hat{P}_x[20] = -2\Phi \tag{23}$$

The compensated phase difference between these terms is:

$$\begin{aligned}\Delta_{ph}(2) &= 2(-\Phi) - (-2\Phi)\\ &= 0\end{aligned} \tag{24}$$

However if M_{xy} is negative, the phases of the same two terms are:

$$\angle \hat{P}_x[10] = \pi - \Phi \tag{25}$$

$$\angle \hat{P}_x[20] = \pi - 2\Phi \tag{26}$$

Which results in a compensated phase difference of:

$$\begin{aligned}\Delta_{ph}(2) &= 2(\pi - \Phi) - (\pi - 2\Phi)\\ &= \pi\end{aligned} \tag{27}$$

Thus the final expression for M_{xy} incorporating both magnitude and sign is:

$$M_{xy} = \begin{cases} \dfrac{|\hat{P}_{nc}[10]|}{C_1}, & \Delta_{ph}(2) = 0 \\ \\ -\dfrac{|\hat{P}_{nc}[10]|}{C_1}, & \Delta_{ph}(2) = \pi \end{cases} \tag{28}$$

where

$$\Delta_{ph}(2) = 2\angle \hat{P}_x[10] - \angle \hat{P}_x[20]$$

This analysis relies on the presence of even harmonics in P_{cal}. In the case of a symmetric waveform with no even harmonics, the compensated phase difference cannot be used to determine the sign of M_{xy}. To see why this is the case consider the first two non-zero terms of the Fourier Series for a symmetric waveform:

$$\text{positive:} \quad a_1 e^{-j\Phi} + a_3 e^{-j3\Phi} \tag{29}$$

$$\text{negative:} \quad -a_1 e^{-j\Phi} - a_3 e^{-j3\Phi} \tag{30}$$

The compensated phase differences between the fundamental and the third harmonic is:

$$\Delta_{ph}(3) = 3\angle a_1 - \angle a_3 \tag{31}$$

Substituting in the phases for each coefficient yields:

$$\text{positive:} \quad 3(-\Phi) - (-3\Phi) = 0 \tag{32}$$

$$\text{negative:} \quad 3(\pi - \Phi) - (\pi - 3\Phi) = 2\pi = 0 \tag{33}$$

The compensated phase difference is the same for both positive and negative waveforms. Intuitively this makes sense because the polarity of a symmetric waveform is ambiguous without a DC component (a_0). This is why the calibration load has a PWM duty cycle of 75% rather than 50%.

B. Multiphase Systems

The preprocessor requires accurate voltage phase information to calculate real (P) and reactive (Q) current. In single phase systems the electric field is always in phase ($\pm\pi$) with the line voltage regardless of the number of conductors. In multiphase systems this is not necessarily the case. In typical three phase systems the voltages of the conductors are mutually offset by 60 degrees resulting in a basis for the electric field that spans $\mathbb{R}2$. To accurately measure phase in these complex environments, a correction factor must be applied to the non-contact voltage sensor output.

Once the voltage waveforms for each phase are known, the calibration procedure to find the M_{xy} coefficients for the non-contact current sensors is identical to the single phase procedure described previously.

To understand the difficulty in voltage reconstruction, consider the output of a non-contact voltage sensor in a three phase system:

$$v_{nc}[n] = S_1 v_1 + S_2 v_2 + S_3 v_3 \tag{34}$$

where S_x is sensitivity to the field produced by voltage v_x. The v_x terms can be expressed as complex sinusoids with the following form:

$$v_x = V_x e^{j\omega t + \Phi_n} \tag{35}$$

Because all of the v_x terms are have the same frequency (ω), Eq 34 can be rewritten as:

$$v_{nc}[n] = \mathcal{R}\{e^{j\omega t}(S_1 V_1 e^{\Phi_1} + S_2 V_2 e^{\Phi_2} + S_3 V_3 e^{\Phi_3})\} \tag{36}$$

The sum of $S_x V_x e^{j\phi_n}$ terms can be represented as a single complex exponential:

$$v_{nc}[n] = \mathcal{R}\{A e^{j\omega t} e^{j\phi}\} \tag{37}$$

where A is the amplitude of the sensor output and ϕ is the phase. Depending on the particular geometry of the system there may be degenerate nodes where the electric fields contributed by each phase sum to zero. In this case $A = 0$ and the sensor should be repositioned.

If the voltage amplitude V is a known constant for all phases, the output of a single non-contact sensor can be used to reconstruct the line voltages:

$$v_1[n] = v_{nc}[n](\tfrac{V}{A} e^{j\psi_1}) \tag{38}$$

$$v_2[n] = v_{nc}[n](\tfrac{V}{A} e^{j\psi_2}) \tag{39}$$

$$v_3[n] = v_{nc}[n](\tfrac{V}{A} e^{j\psi_3}) \tag{40}$$

The only unknowns are the correction terms (ψ_x) which align the measured phase (ϕ) to a particular line phase.

The correction terms can be calculated to within $\pm\pi$ using the calibration load. The calibration load draws only real power so the output of the preprocessor at the PWM frequency should be all P and no Q. However, a misalignment between the line phase and the phase of the non-contact sensor will cause the preprocessor to compute a different ratio of P and Q. The correction factor ψ_n is the rotation required to produce all P and zero Q. This is simply the negative of the power factor angle calculated by the preprocessor:

$$\psi_x = -\tan^{-1}(\frac{Q_x}{P_x}) \tag{41}$$

Due to the interference of background loads, Equation 41 is only valid at the PWM frequency and its harmonics. Using a 200 point DFT to measure the fundamental frequency of P and Q gives the following equation for ψ_x:

$$\psi_x = \tan^{-1}(\frac{\hat{Q}_x[10]}{\hat{P}_x[10]}) \tag{42}$$

It is important to note that this procedure calculates ψ_x to within a factor of $\pm\pi$ which means the sign of the voltage waveform cannot be uniquely determined. However, this does not affect the accuracy of the preprocessor's calculation of real (P) and reactive (Q) power. Conceptually an offset of $\pm\pi$ in ψ_x is equivalent to a current sensor being flipped 180 degrees spatially. Both introduce the same apparent phase difference between sensed voltage and sensed current. Eq 29 associates a sign to each term of the fit matrix $[M]$ to correct for this difference. Therefore the computed real (P) and reactive (Q) power is always correct despite the ambiguity in ψ_x.

C. Rapid Calibration

To more efficiently compute the fit matrix in a multi-conductor system, calibration loads can be connected to each phase and run simultaneously. This is advantageous when multiple phases are available at a single point such as the 240V dryer outlets in residential environments and three phase outlets in industrial environments. Simultaneous calibration requires that each load toggle at a distinct frequency such as 0.5Hz, 3Hz, and 7Hz so that the Fourier coefficients of the fundamentals do not interfere and their harmonics do not overlap.

VII. EXAMPLE 3 PHASE MONITORING

In Figure 16, three non-contact sensor prototypes are mounted with custom enclosures to a three phase power cable. The close proximity of the conductors causes significant overlap in the magnetic fields outside the cable. A visualization of the non-contact current sensor vectors is shown in Figure 17. The "traditional" current sensors form an orthonormal basis shown in dashed lines. Despite the mixed fields, the non-contact sensors are still linearly independent and span $\mathbb{R}3$. After applying the calibration load to each phase, the fit matrix $[K]$ was calculated using the process described. Figure 18 shows a comparison between standard current sensors and the non-contact sensors for loads on all three phases.

VIII. CONCLUSION

Non-contact sensors provide a combined voltage and current monitoring platform in a form factor that attaches easily to circuit breaker panels, power cables, and other power delivery conductors. Because they do not interfere with the physical infrastructure and do not require any service interruption to install it is expected that this type of technology will enable power monitoring in a wide variety of locations where currently such monitors are logistically or physically difficult to deploy. As demand for cost-effective power monitoring systems continues to grow, these nonintrusive sensors remove a barrier to access.

ACKNOWLEDGMENT

The authors gratefully acknowledge the assistance and advice of D. Vickery, C. Schantz, A. Avestruz, K. Surakitbovorn, and Prof. J. Kirtley.

REFERENCES

[1] S. M.-S. B. Foster, "Results from recent real-time feedback studies," American Council Energy-Efficient Economy, Washington, DC, USA, Tech. Rep. B122, Feb. 2012.

[2] E. J. Moniz *et. al.* "Engaging electricity demand," in *MIT Study on the Future of the Electric Grid*. Cambridge, MA, USA: MIT Energy Initiative (MITei), Dec. 2011.

[3] T. Boston, "Declaration on power grid investments," in *Proc. Annu. Meeting GO*, vol. 15. New York, NY, USA, Oct. 2013.

[4] Y.-H. Lin, M.-S. Tsai, and C.-S. Chen, "Applications of fuzzy classification with fuzzy C-means clustering and optimization strategies for load identification in NILM systems," in *Proc. IEEE Int. Conf. Fuzzy Syst. (FUZZ)*, Jun. 2011, pp. 859–866.

[5] H.-H. Chang, K.-L. Chen, Y.-P. Tsai, and W.-J. Lee, "A new measurement method for power signatures of nonintrusive demand monitoring and load identification," *IEEE Trans. Ind. Appl.*, vol. 48, no. 2, pp. 764–771, Mar. 2012.

[6] A. S. Bouhouras, A. N. Milioudis, G. T. Andreou, and D. P. Labridis, "Load signatures improvement through the determination of a spectral distribution coefficient for load identification," in *Proc. 9th Int. Conf. Eur. Energy Market (EEM)*, May 2012, pp. 1–6.

[7] *STJ-340: Four Element Bridge Magnetic Sensor Data Sheet*, Micro Magnetics, Inc., Fall River, MA, USA, May 2010.

[8] *Allegro 1362 Data Sheet*, Allegro MicroSystems, Inc., Melville, NY, USA, Dec. 2013.

[9] M. Julliere, "Tunneling between ferromagnetic films," *Phys. Lett. A*, vol. 54, no. 3, pp. 225–226, 1975.

[10] S. S. P. Parkin *et al.*, "Giant tunnelling magnetoresistance at room temperature with MgO (100) tunnel barriers," *Nature Mater.*, vol. 3, no. 12, pp. 862–867, 2004.

[11] S. Ikeda *et al.*, "Tunnel magnetoresistance of 604% at 300 K by suppression of Ta diffusion in CoFeB/MgO/CoFeB pseudo-spin-valves annealed at high temperature," *Appl. Phys. Lett.*, vol. 93, no. 8, p. 082508, Aug. 2008.

[12] B. Hoberman, *The Emergence of Practical MRAM*, Crocus Technologies, Santa Clara, CA, USA, Tech. Rep., Apr. 2009.

[13] J. Donnal, "Home NILM: A comprehensive non-intrusive load monitoring toolkit," M.S. thesis, Dept. Elect. Eng. Comput. Sci., Massachusetts Institute Technology, Cambridge, MA, USA, Jun. 2013.

[14] S. Leeb, J. Paris, J. Donnal, Z. Remscrim, and S. Shaw, "The sinefit spectral envelope preprocessor," *IEEE Sensors J.*, vol. PP, no. 99, p. 1, 2014.

[15] J. Paris, "A comprehensive system for non-intrusive load monitoring and diagnostics," Ph.D. dissertation, Dept. Elect. Eng. Comput. Sci., Massachusetts Institute Technology, Cambridge, MA, USA, Sep. 2013.

[16] A. V. Oppenheim, A. S. Willsky, and I. T. Young, *Signals and Systems*. Englewood Cliffs, NJ, USA: Prentice-Hall, 1997.

[17] A. V. Oppenheim and R. W. Schafer, *Discrete-Time Signal Processing*. Englewood Cliffs, NJ, USA: Prentice-Hall, 2009.

John S. Donnal (M'13) photograph and biography not available at the time of publication.

Steven B. Leeb (S'89–M'91–SM'01–F'07) photograph and biography not available at the time of publication.